Desalination and Water Treatment
www.deswater.com

doi: 10.5004/dwt.2017.20670

77 (2017) 94–104
May

Fabricating macroporous RuO_2–TiO_2 electrodes using polystyrene templates for high chlorine evolution efficiencies

Tran Le Luu[a], Choonsoo Kim[b], Seonghwan Kim[b], Jiye Kim[b], Jeyong Yoon[b,*]

[a]*Department of Mechatronics and Sensor Systems Technology, Vietnamese German University, Le Lai Street, Hoa Phu Ward, Thu Dau Mot City, Binh Duong Province, Vietnam*
[b]*School of Chemical and Biological Engineering, Institute of Chemical Process (ICP), Asian Institute for Energy, Environment & Sustainability (AIEES), Seoul National University, Gwanakgu, Daehak-dong, Seoul 151-742, Korea, Tel. +82-2-880-8941; Fax: +82-2-876-8911; email: jeyong@snu.ac.kr (J. Yoon)*

Received 6 October 2016; Accepted 16 December 2016

ABSTRACT

In dimensionally stable anodes, RuO_2–TiO_2 has emerged as one of the fundamental anode materials in terms of practical application because of its high stability and catalytic performance toward chlorine evolution. Nevertheless, high chlorine evolution efficiency is still required for an effective chlorine production process. In this study, high chlorine electrocatalytic active RuO_2–TiO_2 electrodes were fabricated using several ranges of polystyrene microsphere templates (0.1, 0.46 and 1.1 μm) resulting in novel three-dimensional ordered macroporous structures. Higher chlorine evolution efficiency was observed in the macroporous RuO_2–TiO_2 electrodes than that in the nontemplated electrode at the same Ru loadings. In particular, a macroporous electrode fabricated with a specific polystyrene size (0.46 μm) exhibited the highest chlorine evolution efficiency in this study indicating the existence of an optimal macropore size for RuO_2–TiO_2 electrodes in the chlorine evolution reaction. This chlorine evolution efficiency could be attributed to the well-developed outer active surface area formed by the optimal pore structure which contributes to the easy mass transfer of chloride ions and removal of produced chlorine gas bubbles. This novel idea strategically provides a new method for preparing inexpensive RuO_2–TiO_2 electrocatalysts with a high electrochemically active surface area, especially the outer active surface area for chlorine evolution.

Keywords: DSA; RuO_2–TiO_2; Macroporous; Chlorine evolution; Outer surface area

1. Introduction

Chlorine, which is generally produced by the chlor-alkali process, is one of the most important chemical species in the chemical, the pharmaceutical industry and for wastewater treatment [1]. In the chlor-alkali process, dimensionally stable anodes (DSA®) have been employed with great success as the electrocatalysts in chlorine evolution in technical electrochemistry [2,3]. These types of anodes usually consist of a Ti support coated by noble metal oxides including RuO_2, IrO_2 or their mixture with valve metal oxide [4–10]. Among these anodes, the RuO_2–TiO_2 binary anode has notably gained interest in the practical application of DSA® due to its high stability and catalytic performance toward chlorine evolution [11,12]. Although the electrochemical chlorine production is a well-established industrial process, it is still necessary to improve the chlorine evolution efficiency of the RuO_2–TiO_2 electrode further and reduce the electrical energy consumption as well [4].

The chlorine evolution efficiency of RuO_2–TiO_2 electrodes depends on several important parameters such as their surface area, composition, annealing temperature, etc. [11–13]. In particular, the surface and pore structure lead to an increased surface area and fast mass transfer is thought to be a key parameter affecting the chlorine evolution efficiency [14,15].

* Corresponding author.

For example, various pathways have been investigated to enhance the surface area of RuO_2 with hollow aerogels [16], vertical nanorods [17–20], nanosheets [21] and nanotubes [22–24]. In particular, the use of a porous framework by virtue of its tiny crystallite dimensions has dramatically emerged as the fundamental method to enhance the surface area of RuO_2 electrodes [25–27]. The porous framework is known to contribute to the high chlorine evolution efficiency of the anode. The pore surface provides improved diffusional access for the electrolyte to reach the electrode surface, and faster transport of the evolving gas from the reactive pore surface due to the enhanced pore connectivity and the formation of gas channels inside [27,28].

In particular, the porous framework can be simply prepared by employing templates with a narrow size distribution as the pore-directing agent, which has been extensively investigated in the synthesis of various nanostructures and exhibit significant promise [29–32]. This process is easy, reliable, versatile, low cost and applicable to a wide variety of electrodes. A previous study showed successful improvement in the oxygen evolution on an IrO_2 macroporous electrode fabricated with an SiO_2 template [33]. The macroporous structure decreases the mass transport resistance compared with porous materials by enabling easy access to the active surface sites for the electrolyte [31–33]. However, a RuO_2–TiO_2 electrode with the macroporous framework that intends to have a controlled pore size without collapse of the wall structure has not been fully investigated for chlorine evolution.

In this study, we report a highly electrocatalytically active RuO_2–TiO_2 electrode for chlorine evolution fabricated by polystyrene (PS) microsphere templates (0.1, 0.46 and 1.1 μm) resulting in novel three-dimensional ordered macroporous structures. The microstructures of the as-prepared electrodes were characterized with scanning electron microscope–energy-dispersive X-ray spectroscopy (SEM–EDS), transmission electron microscopy (TEM) and X-ray diffraction (XRD). The electrochemical properties were examined using the cyclic voltammetry (CV), linear sweep voltammetry (LSV) and total chlorine concentration methods.

2. Experimental setup

2.1. Electrode preparation

The titanium-coated macroporous RuO_2–TiO_2 electrodes were prepared using the thermal decomposition method with several sizes of PS microspheres (0.1, 0.46 and 1.1 μm in diameter) to examine their effect on the macroporous structure including the pore size. Titanium foils (dimensional 30 mm × 20 mm × 0.25 mm, purity 99.7%, Sigma-Aldrich, USA) were utilized as the substrate materials, for which the contaminants were removed by emery paper, degreased in acetone and subsequently etched in boiling concentrated HCl acid at 86°C for 1 h to produce a gray surface with uniform roughness. $RuCl_3$ 42 mg, $TiCl_3$ 72.5 mg (proportion of Ru:Ti was 30:70, % mol/mol), 0.1 mL of hydrogen peroxide solution (30 wt%) and 0.1 g of PS microspheres were dissolved in a solution of 3 mL of ethanol. As a reference, coating without templated macroporosity (nontemplated) was prepared by dissolving Ru:Ti (30:70) as above but without PS microspheres presence. The precursor solution was sonicated for 30 min before it was spread onto the titanium substrates. Next, the electrodes were sintered at 450°C for 1 h to allow for hydrous removal and formation of the metal oxides [34]. To examine the effect of calcination temperature to the PS template, the 0.46-μm PS electrode was also calcinated at 250°C and 350°C for 1 h. The amount of RuO_2 loading in each electrode is approximately 3 mg/cm^2.

2.2. Microstructure characterization

The microstructures, thickness and chemical compositions of the electrode surfaces were characterized using a field emission scanning electron microscope coupled with an EDS system (FE-SEM–EDS, JSM-6701F, JEOL Co., Japan). The SEM–EDS measurements were taken at a working distance of 7 mm and an accelerating voltage of 10 kV. The samples were positioned horizontally [35].

The crystal images were examined using a TEM (JEOL 2000EXII, JEOL Co., Japan). The TEM samples were prepared by scraping off the coating using a sharp knife and then dispersing the powders in isopropyl alcohol. A few drops of this solution were deposited onto carbon-film-coated Cu grids and then analyzed using a microscope. The accelerating voltage, vacuum and tilting angles were 110 kV, 10 Pa, and ±25°C, respectively.

To study the crystallinity of the RuO_2–TiO_2 electrodes, a high-resolution XRD pattern was obtained with the grazing incidence technique on a D8 Discover (Bruker-AXS, Germany) diffractometer (Cu Kα, λ = 1.5406 Å). A scintillation counter detector scanned between 25° and 100° in 2θ with an angle of incidence of 0.5°. The working distance and the accelerating voltage were 12 mm and 25 kV, respectively [36].

N_2 gas adsorption/desorption experiments were performed using a Micromeritics ASAP 2010 analyzer (Micromeritics Instrument Corporation, USA) at 77 K. The BET surface areas and pore size distributions were calculated using the Barrett–Joyner–Halenda (BJH) model on the desorption branch [37,38].

The stability of prepared RuO_2–TiO_2 electrodes was examined using the accelerated stability test (AST) [39,40], with a current density considerably higher than those typically applied in industrial electrochemical conditions (1 A/cm^2, 5 M NaCl, pH = 2, 25°C) to ensure that the desired characteristics of the electrode lifetime via the electrode potential–time dependence was obtained.

2.3. Chlorine evolution and electrochemical measurements

Chlorine was evolved by electrolysis in a two undivided electrodes system under the following conditions (0.1 M NaCl, pH = 2, 16.7 mA/cm^2 and 5 M NaCl, pH = 2, 400 mA/cm^2, t = 10 min). The aqueous active chlorine concentration was determined by the *N*,*N*-diethyl-*p*-phenylenediamine colorimetric method [41]. The experiments were replicated three times, and then the average value with standard deviation was reported. The chlorine current efficiencies and energy consumption were calculated based on Faraday's law and chlorine concentration [42,43]:

$$\mathrm{CF}(\%) = \frac{V \times C \times n \times F}{I \times t} \quad (1)$$

where CF is the current efficiency (%), V is the volume of electrolyte (L), C is the chlorine concentration in the solution (mol/L), n is the number of electron exchanged, F is the Faraday constant (96,485 C/mol), I is the applied current (A) and t is the electrolysis time (s) [42].

In addition:

$$\mathrm{EC} = \frac{756.1 \times E}{CF} \quad (2)$$

where EC is the energy consumption (kWh/ton Cl_2), E is the cell voltage and CF is the current efficiency [43].

Electrochemical characterizations of the RuO_2 electrodes with CV and LSV measurements were performed in a conventional single compartment cell with three electrodes using a computer-controlled potentiostat (PARSTAT 2273A, Princeton Applied Research, USA) [44,45]. To determine the Tafel slopes, LSV (anodic polarization curves) were corrected with compensation of the ohmic drop according to the method assuming that the observed overpotential (V) at any current can be calculated by the uncompensated resistance of the system [46,47]. The volume of the electrolyte solutions in the cell was 150 mL. RuO_2/Ti, Pt (Samsung Chemicals, Korea) and Ag/AgCl (in saturated KCl) were used as the working electrode (anode), the counter electrode (cathode) and the reference electrode, respectively. The CV curves were measured in a solution of 0.5 M H_2SO_4 as the electrolyte with the potential ranging between 0 and 1 V and the scan rate varying from 5 to 320 mV/s. LSV was performed under an acidic condition (pH = 2, 5 M NaCl) in which the chlorine evolution is favored over oxygen evolution [48,49]. The outer surface area was estimated by measuring the voltammetric charge (q) indicating the active accessible Ru sites proposed in previous studies [50,51]. The voltammetric charge recorded in the potential range in the cyclic voltammograms can be described by a pseudo-capacitive reaction ($RuO_x(OH)_y$ + $zH^+ + ze^- \rightarrow RuO_{x-z}(OH)_{y+z}$) which consists of coupled redox transitions involving proton exchange at a broad reversible peak of approximately 0.6 V vs. Ag/AgCl. To observe the stability with pseudo-capacitance, CV and voltammetric charges of the electrodes were also recorded at the scan rate 20 mV/s after the 1st, 500th and 1,000th cycles.

3. Results and discussion

3.1. Surface analysis

Fig. 1 shows the SEM (a) and TEM (b) images of the RuO_2–TiO_2 electrodes fabricated for several different sizes of the PS microspheres (diameters of 0.1, 0.46 and 1.1 μm) compared with the nontemplated electrode. As shown in Fig. 1(a), the RuO_2–TiO_2 electrodes (PS 0.1, 0.46 and 1.1 μm) clearly exhibited three-dimensional uniform macroporous structures. In addition, the macropores on the RuO_2–TiO_2 electrodes appeared to be smaller than the PS microspheres. In other words, the 0.1, 0.46 and 1.1 μm diameters of the PS microspheres led to pore sizes of ca. 0.05, 0.2 and 0.6 μm, respectively. This observation can be explained by the contraction of the microspheres during the sintering process [26–28]. Furthermore, the distinct surface morphology of the macroporous electrodes (PS 0.1, 0.46 and 1.1 μm) and the nontemplated electrode with its irregularly shaped aggregates (11–20 nm) and no macroporous structure was also clearly observed in the TEM images (Fig. 1(b)). This observation is in accord with the results of the SEM images in Fig. 1(a). The results in Fig. 1 suggest that PS microspheres as templates play a fundamental role in the synthesis of macroporous RuO_2–TiO_2 electrodes. However, the thicknesses of the coating layers measured by cross-sectional SEM were approximately 7 μm (Fig. S1 in supplementary information), excluding the effect on the electrocatalyst resulting from the different thicknesses of the oxide layer. In addition, the compositions of Ru of all the macroporous and nontemplated RuO_2–TiO_2 electrodes measured using EDS also appeared to be similar, excluding the effect on the electrocatalyst resulting from the different Ru quantities in the oxide layer. Note that the percentage of Ru on PS 0.1, 0.46, 1.1 μm and the

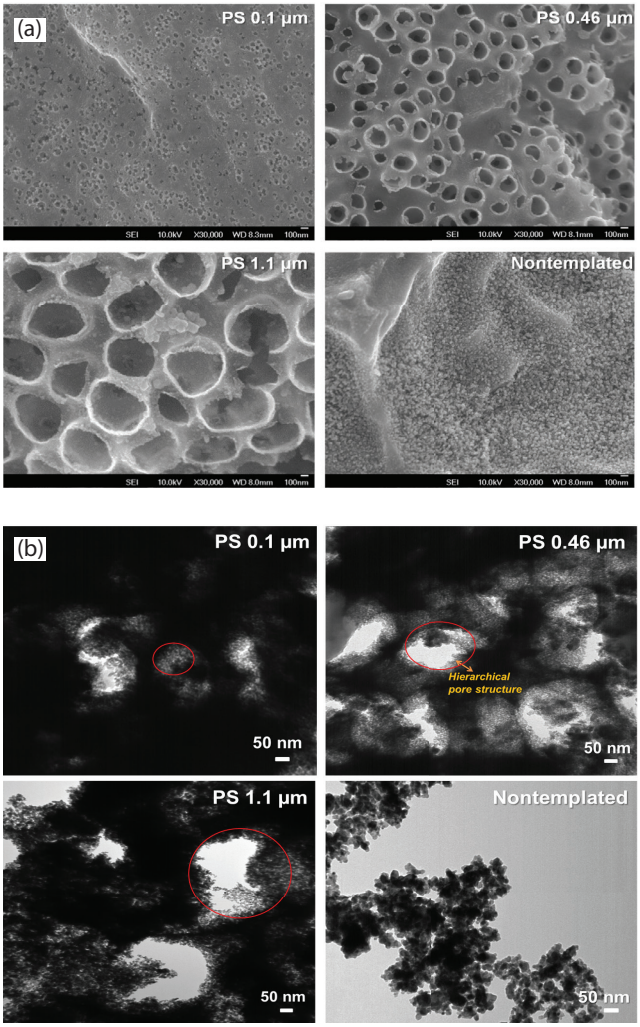

Fig. 1. SEM (a) and TEM (b) images of the macroporous RuO_2–TiO_2 electrodes fabricated with several ranges of the PS sizes (diameter of 0.1, 0.46 and 1.1 μm) in comparison with that of the nontemplated RuO_2–TiO_2 electrode.

nontemplated electrodes were: 8.7%, 8.6%, 8.1% and 8.4%, respectively.

The effect of the heat treatment step on polysterene microsphere (as expressed by C%) was examined by EDS measurement at several calcination temperatures (250°C, 350°C and 450°C). Table 1 presents the C% remaining on the macroporous RuO_2–TiO_2 electrodes at several calcination temperatures. As presented in Table 1, the C% decreases with the increase of calcination temperature, falling from 27.2% at 250°C to <1% at 450°C, for all of the prepared macroporous electrodes, indicating that the PS is well removed at 450°C. This observation is consistent with the results of the previous studies [52–54]. The results in Table 1 were clearly supported by the SEM images (Fig. S2 in supplementary information).

Fig. 2 shows the XRD spectra of the macroporous and nontemplated RuO_2–TiO_2 electrodes. As shown in Fig. 2, the (110) rutile peak was observed at approximately 27.8° which exists between the reference peak of the pure rutile TiO_2 (110) (27.4°) and the peak of the rutile RuO_2 (110) phase (28.05°), indicating that the solid solution of RuO_2 and TiO_2 was formed. The formation of a solid solution is presumed to contribute to the stability of electrode [55,56]. Alternatively, the formation of isolated rutile-type RuO_2 and TiO_2 is explained by the effect of water in H_2O_2 solution (30%). For example, water induces the hydrolysis of $TiCl_3$ to form $Ti(OH)_x$ at room temperature, while crystalline $RuO_2{\cdot}xH_2O$ is formed at higher decomposition temperature [57]. This process is further supported by the report that the deviations from stoichiometry are accommodated in TiO_2 by the formation of crystallographic shear planes, whereas there is no evidence for similar defects in nonstoichiometric RuO_2 [56,58]. Because X-rays can penetrate through the coating layers, the absorption peaks of Ti metal substrates were also observed. No evidence of an Ru metallic peak was observed, which means that the electrodes are high-purity phase structures. Their average crystallite sizes calculated by the Scherrer equation [36] for the peaks of (110) were approximately 15 nm. This result indicates that both the macroporous and nontemplated RuO_2–TiO_2 electrodes possessed similar crystallite structure and sizes despite significantly different surface morphologies.

Table 1
C% contamination on the macroporous RuO_2–TiO_2 electrodes fabricated at several calcination temperatures (250°C, 350° and 450°C) for different PS sizes (diameter of 0.1, 0.46 and 1.1 μm) in comparison with that of the nontemplated RuO_2–TiO_2 electrode

Sample	C (%)
250°C (PS 0.46 μm)	27.2
350°C (PS 0.46 μm)	9.8
450°C (PS 0.46 μm)	0.8
450°C (PS 0.1 μm)	0.6
450°C (PS 1.1 μm)	0.9
450°C (nontemplated)	0.4

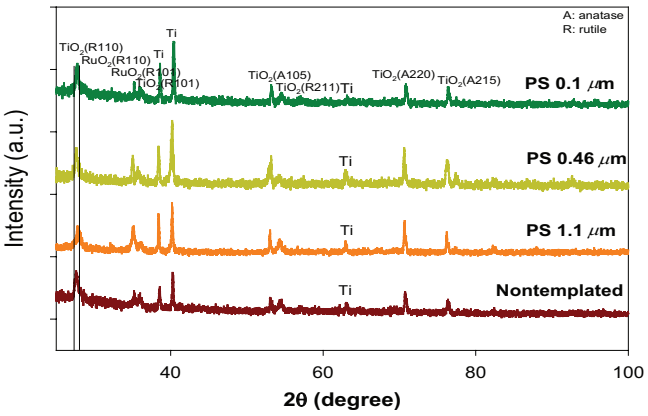

Fig. 2. XRD patterns of the macroporous RuO_2–TiO_2 electrodes fabricated with several ranges of the PS sizes (diameter of 0.1, 0.46 and 1.1 μm) in comparison with that of the nontemplated RuO_2–TiO_2 electrode.

3.2. Chlorine evolution on the ordered macroporous RuO_2–TiO_2 electrodes

Fig. 3 shows measurements via LSV for the macroporous and nontemplated RuO_2–TiO_2 electrodes. There are two important observations in Fig. 3. First, all of the macroporous RuO_2–TiO_2 electrodes showed a higher current density as a result of the charge transfer reaction in chlorine evolution compared with the nontemplated electrode. Second, among the macroporous electrodes, PS 0.46 μm, but not PS 0.1 and 1.1 μm, exhibited the highest current density, indicating the existence of an optimal macropore size for RuO_2–TiO_2 electrodes. Under this condition for the LSV measurement, oxygen evolution is suppressed, thereby increasing the oxygen overpotential and selectivity for chlorine evolution [48,49].

The polarization curves of the RuO_2–TiO_2 electrodes were presented in Fig. 4, and a representative LSV curve of PS 0.1 μm electrode before and after IR correction was provided in the inset. As seen in Fig. 4, the Tafel slope of the PS 0.1, 0.46 and 1.1 μm electrodes of 31 mV/dec, 30 mV/dec and 34 mV/dec, respectively, were lower than that of the nontemplated electrode (40 mV/dec). This result is consistent with the previous studies, in which the Tafel slope of normal or commercial electrode was reported as typically 40–60 mV/dec for

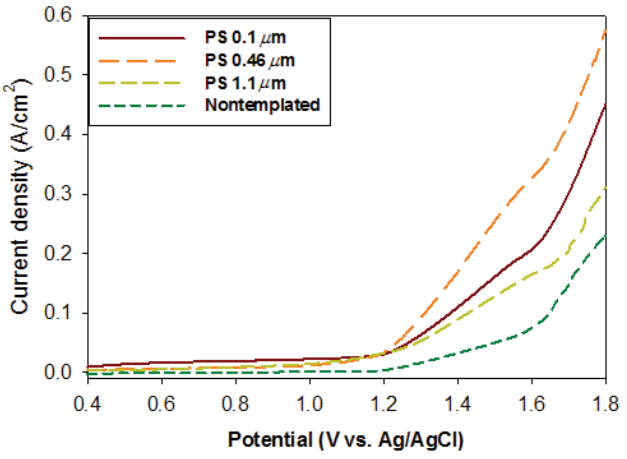

Fig. 3. Linear sweep voltammetry (5 M NaCl, pH = 2) of the macroporous RuO_2–TiO_2 electrodes fabricated with several ranges of the PS sizes (diameter of 0.1, 0.46 and 1.1 μm) in comparison with that of the nontemplated RuO_2–TiO_2 electrode.

an RuO_2-based electrode [43,51]. The lower Tafel slopes of the macroporous RuO_2–TiO_2 electrodes indicate higher electrocatalytic with chlorine evolution than that of the nontempalated electrode. This result can be explained by the facilitated diffusion or the mass transport of the reactive species and products through the macroporous frameworks.

Table 2 presents the chlorine current efficiencies and energy consumption of the macroporous RuO_2–TiO_2 electrodes fabricated for several ranges of the PS sizes (diameter of 0.1, 0.46 and 1.1 μm) and without the PS template (nontemplated) or commercial electrode at two different electrolysis conditions. As seen in Table 2, the current efficiencies at a high concentration (5 M NaCl) and high current density (400 mA/cm²) are much higher than those at a low concentration (0.1 M NaCl) and low current density (16.7 mA/cm²). For example, the current efficiencies at a high concentration (5 M NaCl) and high current density (400 mA/cm²) were approximately 90%–98%, while the current efficiencies at low concentration (0.1 M NaCl) and low current density (16.7 mA/cm²) were approximately 49%–75%. These results agree with the previous studies, which reported current efficiencies for chlorine evolution reaction in dilute chloride solutions of 8%–45% depending upon the experimental conditions, while at higher brine concentration and current density, the reported current efficiencies were approximately 90%–92% at a commercial electrode [59–61]. The macroporous RuO_2–TiO_2 electrodes increase the chlorine current efficiency compared with the nontemplated electrode in the chlor-alkali industry. In addition, the macroporous of RuO_2–TiO_2 electrodes also reduce the energy consumption (~200 kWh/ton Cl_2 in case of PS 0.46 μm) in the chlor-alkali industry. The energy consumption of a normal electrode at chlor-alkali condition was reported in the literature to be in the range of 2,300–2,600 (kWh/ton Cl_2) [4,43]. The lower current efficiency and higher energy consumption at the condition of lower brine concentration and current density reveal that the interference of oxygen evolution.

3.3. Surface area of the ordered macroporous RuO_2–TiO_2 electrodes

Fig. 5 shows the voltammetric charge obtained from the cyclic voltammograms with the scan rate (5–320 mV/s) within a potential range of 0.0–1.0 V in 0.5 M H_2SO_4 (Fig. S3 in supplementary information) to estimate the total and outer surface areas of the RuO_2–TiO_2 electrodes [50,51]. The total voltammetric charge including both the inner and outer active surfaces can be measured at a low scan rate. Alternatively,

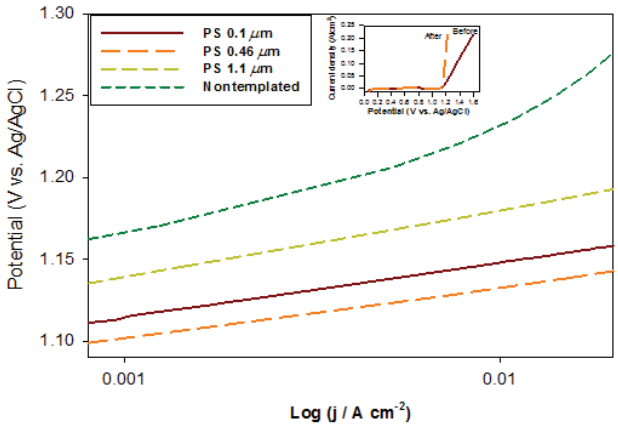

Fig. 4. The polarization curves of the macroporous RuO_2–TiO_2 electrodes fabricated with several ranges of the PS sizes (diameter of 0.1, 0.46 and 1.1 μm) in comparison with that of the nontemplated RuO_2–TiO_2 electrode under chlor-alkali condition of 5 M NaCl, pH = 2 (inset: the representative LSV curve of PS 0.1 μm electrode before and after IR correction).

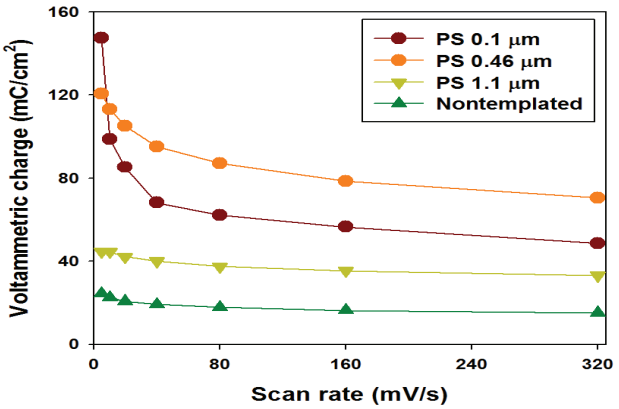

Fig. 5. Voltammetric charges of the macroporous RuO_2–TiO_2 electrodes fabricated with several ranges of the PS sizes (diameter of 0.1, 0.46 and 1.1 μm) in comparison with that of the nontemplated RuO_2–TiO_2 electrode.

Table 2
Chlorine current efficiencies and energy consumption of the macroporous RuO_2–TiO_2 electrodes fabricated with several ranges of the PS sizes (diameter of 0.1, 0.46 and 1.1 μm) in comparison with that of the nontemplated RuO_2–TiO_2 electrode at different electrolysis conditions

Electrode	Current efficiency (%)		Energy consumption (kWh/ton Cl_2)	
	5 M NaCl, pH = 2, 400 mA/cm²	0.1 M NaCl, pH = 2, 16.7 mA/cm²	5 M NaCl, pH = 2, 400 mA/cm²	0.1 M NaCl, pH = 2, 16.7 mA/cm²
PS 0.1 μm	97	70	2,251	2,925
PS 0.46 μm	98	75	2,229	2,721
PS 1.1 μm	94	62	2,317	3,274
Nontemplated	90	49	2,415	4,140

the outer voltammetric charge can be obtained at a high scan rate [50]. Note that, in Fig. 5, the order of the total surface area for the electrodes was different from that of the outer surface area. That is, the total surface area was in decreasing order of PS 0.1, 0.46, 1.1 μm and the nontemplated electrode, while the outer surface areas was in decreasing order of PS 0.46, 0.1, 1.1 μm and the nontemplated electrode. More details of the electrochemically active surface area are provided in Table S1 in supplementary information. Thus, the outer surface area was in good agreement with the results of the chlorine evolution efficiency for the macroporous RuO_2–TiO_2 electrodes, indicating that the outer surface area plays a more critical role in enhancing the chlorine evolution efficiency than that of the total surface area, and the pore size can affect the optimal development of the outer surface area. As mentioned earlier, the reason for this behavior could be because of the increased mass transfer or the easy removal of chlorine gas bubbles based on the well-developed outer structure of the macroporous electrodes because the chlorine evolution reaction rate is notably fast and thermodynamically reversible [11,62–64]. Furthermore, under intensive gas evolution, the inner surface was found to be blocked by adherent gas bubbles and becomes partially inactive for chlorine evolution [65–67].

Table 3 shows a summary of the average pore size, pore volume and surface area of the prepared electrodes. As presented in Table 3, the average pore diameters of macroporous RuO_2–TiO_2 electrodes fabricated with PS 0.1, 0.46 and 1.1 μm, are similar, regardless of the PS template sizes: 25, 26 and 27 nm, respectively. These diameters of the macroporous RuO_2–TiO_2 electrodes were larger than that of the nontemplated RuO_2–TiO_2 electrode (~18 nm). The BET surface areas and pore volumes of the RuO_2–TiO_2 macroporous electrodes greatly decrease with the increase of the PS template sizes from 0.1 to 1.1 μm. For example, the specific surface areas of the RuO_2–TiO_2 macroporous electrodes fabricated with PS sizes of 0.1, 0.46 and 1.1 μm were 233, 178 and 88 m^2/g, while the surface area of the nontemplated electrode was much lower, 41 m^2/g. These results are consistent with the previous studies indicating that RuO_2-based electrodes ranged from 42 to 263 m^2/g, depending on the calcination temperature and the fabrication condition [25,68–70]. It is important to recognize that the largest surface area may not ensure for the highest chlorine evolution efficiency.

Table 3
BET surface areas of the macroporous RuO_2–TiO_2 electrodes fabricated with several ranges of the PS sizes (diameter of 0.1, 0.46 and 1.1 μm) in comparison with that of the nontemplated RuO_2–TiO_2 electrode

Sample	Average BJH pore size (nm)	Pore volume (cc/g)	BET surface area (m^2/g)
PS 0.1 μm	25	0.78	233
PS 0.46 μm	26	0.56	178
PS 1.1 μm	27	0.33	88
Nontemplated	18	0.09	41

3.4. The stability of the ordered macroporous RuO_2–TiO_2 electrodes

As mentioned in the previous section, the solid solution of RuO_2 and TiO_2, which contribute to the stability of electrodes against chlorine evolution, was formed in all of the prepared electrodes. To examine this phenomenon further, the stability test was conducted in terms of chlorine evolution and pseudo-capacitive reaction. ASTs performed for long hours at high current density (1 A/cm^2) were applied for all the prepared electrodes and their results are presented in Fig. 6. As shown in Fig. 6, the highest stability was observed in nontemplated macroporous RuO_2–TiO_2 electrodes (maximum lifetime 14 h) among all the prepared electrodes. This level of stability is consistent with the previous studies on the RuO_2-based electrodes [71–75]. However, note that the stability of the macroporous electrodes decrease a little bit with the increase of pore sizes under the same electrolysis condition, but still keep the high stability compared with the nontemplated electrode. For example, the lifetime of the electrode with PS sizes of 0.1, 0.46 and 1.1 μm were 13.5, 13 and 11 h, respectively. This observation can be explained by the insulating TiO_2 grains being formed on the interface via oxidation of the Ti substrate as the electrolyte penetrates through open pores toward the substrate. In addition, as the pore sizes increase, the connectivity between RuO_2–TiO_2 nanoparticles becomes looser and the erosion of the catalyst coating is induced [35,39,40]. In addition, as the pore structure of the nontemplated electrode is more compact and the penetration of the electrolyte toward the titanium substrate is limited. Thus, the structure allows for reduced nonconductive intermediate TiO_2 layer formation as compared with the macroporous RuO_2–TiO_2 electrodes [35,40]. The research to increase the lifetime of macroporous RuO_2–TiO_2 electrodes during the real electrolysis is now under processing.

Next, the stability in terms of the pseudo-capacitive property on the electrodes was tested over 1,000 cycles in H_2SO_4

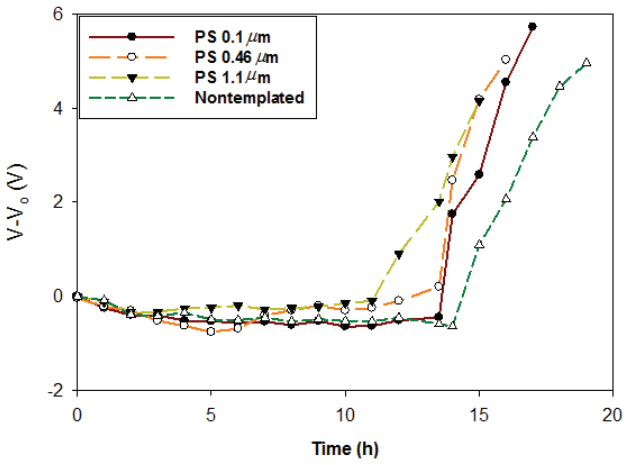

Fig. 6. The AST of the macroporous RuO_2–TiO_2 electrodes fabricated with several ranges of the PS sizes (diameter of 0.1, 0.46 and 1.1 μm) in comparison with that of the nontemplated RuO_2–TiO_2 electrode. Experimental conditions: 5 M NaCl, pH = 2, 25°C, 1 A/cm^2.

0.5 M at 0–1.0 V vs. Ag/AgCl KCl (saturated) at 20 mV/s and the results at the 1st, 500th and 1,000th cycles are presented in Figs. 7(a) and (b). As seen in Figs. 7(a) and (b), the pseudo-capacitive property was retained during 1,000 cycles of operation. Less than 10% of the decrease of voltammetric charges was observed in all the electrodes. Note that, the pseudo-capacitive property of PS 0.1, 0.46, 1.1 μm and nontemplated RuO_2–TiO_2 electrodes decreased by approximately 3.3%, 4.6%, 9.5% and 1.4%, respectively. This result indicates that the proton absorption/desorption reaction ($RuO_x(OH)_y$ + $zH^+ + ze^- \rightarrow RuO_{x-z}(OH)_{y+z}$) did not affect the stability of the RuO_2–TiO_2 electrodes.

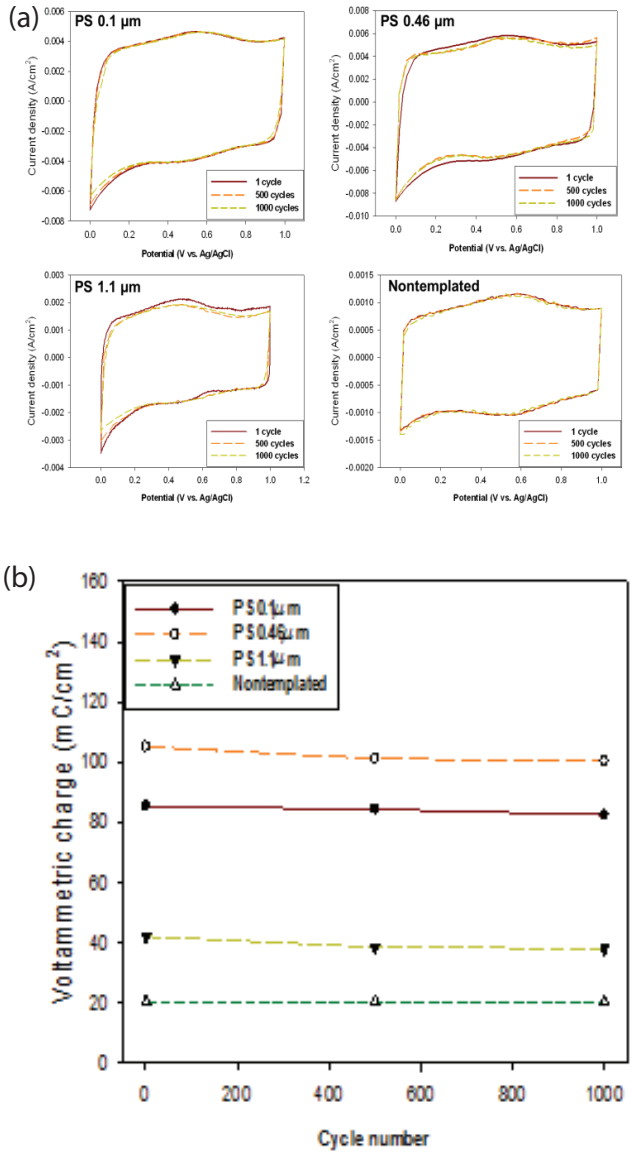

Fig. 7. The CVs (a) and voltammetric charges (b) of the macroporous RuO_2–TiO_2 electrodes fabricated with several ranges of the PS sizes (diameter of 0.1, 0.46 and 1.1 μm) in comparison with that of the nontemplated RuO_2–TiO_2 electrode (0.5 M H_2SO_4, 20 mV/s).

4. Conclusions

In this study, we fabricated highly electrocatalytically active RuO_2–TiO_2 electrodes for chlorine evolution based on a structural ordered macroporous framework using PS microsphere templates (0.1–1.1 μm). A significant higher chlorine evolution efficiency was observed in the macroporous RuO_2–TiO_2 electrodes than that in the nontemplated electrode at the same Ru loadings. Interestingly, in the macroporous RuO_2–TiO_2 electrode with the specific templated pore size of PS 0.46 μm, and not those of PS 1.1 or 0.1 μm, the outer surface area was the most well-developed, and led to the highest chlorine evolution efficiency in this study, indicating the existence of an optimal macropore size for an effective chlorine evolution reaction. This result could be attributed to the structural properties of the macroporous electrodes, which provide easy mass transfer and removal of chlorine gas bubbles and good control over the pore size and pore walls connectivity. The macroporous RuO_2–TiO_2 electrodes can be considered as promising anode materials with high chlorine evolution efficiency in the future chlor-alkali industry.

Acknowledgments

This research was supported by a grant (code 16IFIP-B065893-04) from Industrial Facilities and Infrastructure Research Program funded by Ministry of Land, Infrastructure and Transport of Korean government.

References

[1] T.L. Luu, J. Kim, J. Yoon, Physicochemical properties of RuO_2 and IrO_2 electrodes affecting chlorine evolutions, J. Ind. Eng. Chem., 21 (2014) 400–404.
[2] S. Trasatti, Electrocatalysis: understanding the success of DSA®, Electrochim. Acta, 45 (2000) 2377–2385.
[3] S. Trasatti, Electrocatalysis in the anodic evolution of oxygen and chlorine, Electrochim. Acta, 29 (1984) 1503–1512.
[4] H. Over, Atomic scale insights into electrochemical versus gas phase oxidation of HCl over RuO_2-based catalysts: a comparative review, Electrochim. Acta, 93 (2013) 314–333.
[5] V. Srinivasan, P. Arora, P. Ramadass, Report on the electrolytic industries for the year 2004, J. Electrochem. Soc., 153 (2006) K1–K14.
[6] V. Petrykina, K. Macounova, M. Okube, S. Mukerjee, P. Krtil, Local structure of Co doped RuO_2 nanocrystalline electrocatalytic materials for chlorine and oxygen evolution, Catal. Today, 202 (2013) 63–69.
[7] K. Exner, J. Anton, T. Jacob, H. Over, Chlorine evolution reaction on RuO_2(110): *ab initio* atomistic thermodynamics study – Pourbaix diagrams, Electrochim. Acta, 120 (2014) 460–466.
[8] S. Trasatti, Physical electrochemistry of ceramic oxides, Electrochim. Acta, 36 (1991) 225–241.
[9] H. Hansen, I. Man, F. Studt, F. Pedersen, T. Bligaard, J. Rossmeisl, Electrochemical chlorine evolution at rutile oxide (110) surfaces, Phys. Chem. Chem. Phys., 12 (2010) 283–290.
[10] J. Jirkovský, H. Hoffmannová, M. Klementová, P. Krtil, Particle size dependence of the electrocatalytic activity of nanocrystalline RuO_2 electrodes, J. Electrochem. Soc., 153 (2006) E111–E118.
[11] T. Luu, C. Kim, J. Kim, S. Kim, J. Yoon, The effect of preparation parameters in thermal decomposition of RuO_2 electrodes on chlorine electro-catalytic activity, Bull. Korean Chem. Soc., 36 (2015) 1411–1417.
[12] R. Burrows, D. Denton, J. Harrision, Chlorine and oxygen evolution on various compositions of RuO_2/TiO_2 electrodes, Electrochim. Acta, 23 (1978) 493–500.

[13] D. Denton, J. Harrison, R. Knowles, Chlorine evolution and reduction on RuO_2/TiO_2 electrodes, Electrochim. Acta, 24 (1979) 521–527.
[14] R. Liu, J. Duay, S. Lee, Heterogeneous nanostructured electrode materials for electrochemical energy storage, Chem. Commun., 47 (2011) 1384–1404.
[15] J. Tiwari, R. Tiwari, K. Kim, Zero-dimensional, one-dimensional, two-dimensional and three-dimensional nanostructured materials for advanced electrochemical energy devices, Prog. Mater. Sci., 57 (2012) 724–803.
[16] X. Wu, Y. Zeng, H. Gao, J. Su, J. Liu, Z. Zhu, Template synthesis of hollow fusiform $RuO_2.xH_2O$ nanostructure and its supercapacitor performance, J. Mater. Chem., 1 (2013) 469–472.
[17] J. Chou, Y. Chen, M. Yang, Y. Chen, C. Lai, H. Chiu, C. Lee, Y. Chueh, J. Gan, RuO_2/MnO_2 core–shell nanorods for supercapacitors, J. Mater. Chem., 1 (2013) 8753–8759.
[18] D. Music, J. Breunung, S. Mráz, J. Schneider, Role of RuO_3 for the formation of RuO_2 nanorods, Appl. Phys. Lett., 100 (2012) 033108.
[19] G. Zhao, L. Zhang, K. Sun, H. Li, Free-standing $Pt@RuO_2.xH_2O$ nanorod arrays on Si wafers as electrodes for methanol electro-oxidation, J. Power Sources, 245 (2014) 892–897.
[20] M. Kang, Y. Lee, H. Jung, J. Shim, N. Lee, J. Baik, S. Lee, C. Lee, Y. Lee, M. Kim, Single carbon fiber decorated with RuO_2 nanorods as a highly electrocatalytic sensing element, Anal. Chem., 84 (2012) 9485–9491.
[21] A. Ananth, S. Dharaneedharan, M. Gandhi, M. Heo, Y. Mok, Novel RuO_2 nanosheets – facile synthesis, characterization and application, Chem. Eng. J., 223 (2013) 729–736.
[22] A. Ponrouch, S. Garbarino, E. Bertin, D. Guay, Ultra high capacitance values of $Pt@RuO_2$ core–shell nanotubular electrodes for microsupercapacitor applications, J. Power Sources, 221 (2013) 228–231.
[23] K. Xiong, Z. Deng, L. Li, S. Chen, M. Xia, L. Zhang, X. Qi, W. Ding, S. Tan, Z. Wei, Sn and Sb co-doped Ru-Ti oxides supported on TiO_2 nanotubes anode for selectivity toward electrocatalytic chlorine evolution, J. Appl. Electrochem., 43 (2013) 847–854.
[24] H. Cao, D. Lu, J. Lin, Q. Ye, J. Wu, G. Zheng, Novel Sb-doped ruthenium oxide electrode with ordered nanotube structure and its electrocatalytic activity toward chlorine evolution, Electrochim. Acta, 91 (2013) 234–239.
[25] S. Oh, L. Nazar, Direct synthesis of electroactive mesoporous hydrous crystalline RuO_2 templated by a cationic surfactant, J. Mater. Chem., 20 (2010) 3834–3839.
[26] C. Sassoye, C. Laberty, H. Khanh, S. Cassaignon, C. Boissiere, M. Antonietti, C. Sanchez, Block-copolymer-templated synthesis of electroactive RuO_2-based mesoporous thin films, Adv. Funct. Mater., 19 (2009) 1922–1929.
[27] N. Menzel, E. Ortel, K. Mette, R. Kraehnert, P. Strasser, Dimensionally stable $Ru/Ir/TiO_2$ anodes with tailored mesoporosity for efficient electrochemical chlorine evolution, ACS Catal., 3 (2013) 1324–1333.
[28] E. Ortel, T. Reier, P. Strasser, R. Kraehnert, Mesoporous IrO_2 films templated by PEO-PB-PEO block-copolymers: self-assembly, crystallization behavior, and electrocatalytic performance, Chem. Mater., 23 (2011) 3201–3209.
[29] N. Menzel, E. Ortel, R. Kraehnert, P. Strasser, Electrocatalysis using porous nanostructured materials, Chem. Phys. Chem., 13 (2012) 1385–1394.
[30] F. Jiang, T. Zheng, Y. Yang, Preparation and electrochromic properties of tungsten oxide and iridium oxide porous films, J. Non-Cryst. Solids, 354 (2008) 1290–1293.
[31] O. Velev, E. Kaler, Structured porous materials via colloidal crystal templating: from inorganic oxides to metals, Adv. Mater., 12 (2000) 531–534.
[32] N. Petkovich, A. Stein, Controlling macro- and mesostructures with hierarchical porosity through combined hard and soft templating, Chem. Soc. Rev., 42 (2013) 3721–3739.
[33] W. Hu, Y. Wang, X. Hu, Y. Zhou, S. Chen, Three-dimensional ordered macroporous IrO_2 as electrocatalyst for oxygen evolution reaction in acidic medium, J. Mater. Chem., 22 (2012) 6010–6016.
[34] R. Kotz, S. Stuck, Stabilization of RuO_2 by IrO_2 for anodic oxygen evolution in acid media, Electrochim. Acta, 31 (1986) 1311–1316.
[35] V. Panic, A. Dekanski, S. Milonjic, R. Atanasoski, B. Nikolic, RuO_2–TiO_2 coated titanium anodes obtained by the sol–gel procedure and their electrochemical behaviour in the chlorine evolution reaction, Colloids Surf., A, 157 (1999) 269–274.
[36] C. Malmgren, A.K. Eriksson, A. Cornell, J. Backtrom, S. Eriksson, H. Olin, Nanocrystallinity in RuO_2 coatings — influence of precursor and preparation temperature, Thin Solid Films, 518 (2010) 3615–3618.
[37] Y. Kim, C. Kim, J. Yi, Synthesis of tailored porous alumina with a bimodal pore size distribution, Mater. Res. Bull., 39 (2004) 2103–2112.
[38] S. Tabata, Y. Isshiki, M. Watanabez, Inverse opal carbons derived from a polymer precursor as electrode materials for electric double-layer capacitors, J. Electrochem. Soc., 155 (2008) K42–K49.
[39] A. Pilla, E. Cobo, M. Duarte, D. Salinas, Evaluation of anode deactivation in chlor-alkali cells, J. Appl. Electrochem., 27 (1997) 1283–1289.
[40] V. Panic, A. Dekanski, M. Stankovic, S. Milonjic, B. Nikoli, On the deactivation mechanisms of RuO_2–TiO_2/Ti anodes prepared by the sol–gel procedure, J. Electroanal. Chem., 579 (2005) 67–76.
[41] APHA, Standard Methods for the Examination of Water and Wastewater, 21st ed., American Public Health Association, Washington, D.C., USA, 2005, pp. 4–46.
[42] J. Choi, S. Shim, J. Yoon, Design and operating parameters affecting an electrochlorination system, J. Ind. Eng. Chem., 19 (2013) 215–219.
[43] T. O'Brien, T. Bommaraju, F. Hine, Handbook of Chlor-Alkali Technology, Springer, USA, 2005, p. 166.
[44] A. Bard, L. Faulkner, Electrochemical Methods: Fundamentals and Applications, 2nd ed., Wiley, New York, 2001, pp. 200–217.
[45] J. Jeong, C. Kim, J. Yoon, The effect of electrode material on the generation of oxidants and microbial inactivation in the electrochemical disinfection processes, Water Res., 43 (2009) 895–901.
[46] A. Kapałka, G. Foti, C. Comninellis, Determination of the Tafel slope for oxygen evolution on boron-doped diamond electrodes, Electrochem. Commun., 10 (2008) 607–610.
[47] M. Santana, L. Faria, Oxygen and chlorine evolution on RuO_2 + TiO_2 + CeO_2 + Nb_2O_5 mixed oxide electrodes, Electrochim. Acta, 51 (2006) 3578–3585.
[48] J. Bennett, Electrodes for generation of hydrogen and oxygen from seawater, Int. J. Hydrogen Energy, 5 (1980) 401–408.
[49] H.K. Abdel-aal, S.M. Sultan, I.A. Hussein, Parametric study for saline water electrolysis: part II – chlorine evolution, selectivity and determination, Int. J. Hydrogen Energy, 18 (1993) 545–551.
[50] S. Ardizzone, G. Fregonara, S. Trasatti, "Inner" and "outer" active surface of RuO_2 electrodes, Electrochim. Acta, 35 (1990) 263–267.
[51] V. Trieu, B. Schleya, H. Nattera, J. Kintrup, A. Bulan, R. Hempelmann, RuO_2-based anodes with tailored surface morphology for improved chlorine electro-activity, Electrochim. Acta, 78 (2012) 188–194.
[52] L. Chen, L. Xie, M. Wang, X. Ge, Preparation of three-dimensional inverse opal SnO_2/graphene composite microspheres and their enhanced photocatalytic activities, J. Mater. Chem. A, 3 (2015) 2991–2998.
[53] M. Zhou, H. Wu, J. Bao, L. Liang, X. Lou, Y. Xie, Ordered macroporous $BiVO_4$ architectures with controllable dual porosity for efficient solar water splitting, Angew. Chem. Int. Ed., 52 (2013) 8579–8583.
[54] S. Woo, K. Dokko, H. Nakano, K. Kanamura, Preparation of three dimensionally ordered macroporous carbon with mesoporous walls for electric double-layer capacitors, J. Mater. Chem., 18 (2008) 1674–1680.
[55] Y. Chen, Phase structure and microstructure of a nanoscale TiO_2–RuO_2–IrO_2–Ta_2O_5 anode coating on titanium, J. Am. Ceram. Soc., 91 (2008) 4154–4157.

[56] W. Gerrard, B. Steele, Microstructural investigations on mixed RuO_2-TiO_2 coatings, J. Appl. Electrochem., 8 (1978) 417–425.
[57] C. Hu, Y. Yang, T. Lee, Microwave-assisted hydrothermal synthesis of $RuO_2.xH_2O$–TiO_2 electrodes for high power supercapacitors, Electrochem. Solid-State Lett., 13 (2010) A173–A176.
[58] M. Colomer, J. Jurado, Structural, microstructural, and electrical transport properties of TiO_2–RuO_2 ceramic materials obtained by polymeric sol–gel route, Chem. Mater., 12 (2000) 923–930.
[59] A. Kuhn, C. Mortimer, The efficiency of chlorine evolution in dilute brines on ruthenium dioxide electrodes, J. Appl. Electrochem., 2 (1972) 283–287.
[60] G. Qin, Z. Li, X. Chen, A. Russell, An experimental study of an NaClO generator for anti-microbial applications in the food industry, J. Food Eng., 54 (2002) 111–118.
[61] F. Hine, M. Yasuda, T. Noda, T. Yoshida, J. Okuda, Electrochemical behavior of the oxide-coated metal anodes, J. Electrochem. Soc., 126 (1979) 1439–1445.
[62] L.D. Burke, J.F. O'Neill, Some aspects of the chlorine evolution reaction at Ruthenium dioxides anodes, J. Electroanal. Chem., 101 (1979) 341–349.
[63] S. Trasatti, Progress in the understanding of the mechanism of chlorine evolution at oxide electrodes, Electrochim. Acta, 32 (1987) 369–382.
[64] S. Ardizzone, A. Carugati, G. Lodi, S. Trasatti, Surface structure of ruthenium dioxide electrodes and kinetics of chlorine evolution, J. Electrochem. Soc., 129 (1982) 1689–1693.
[65] R. Chen, V. Trieu, A.R. Zeradjanin, H. Natter, D. Teschner, J. Kintrup, A. Bulan, W. Schuhmann, R. Hempelmann, Microstructural impact of anodic coatings on the electrochemical chlorine evolution reaction, Phys. Chem. Chem. Phys., 14 (2012) 7392–7399.
[66] R. Chen, V. Trieu, H. Natter, J. Kintrup, A. Bulan, R. Hempelmann, Wavelet analysis of chlorine bubble evolution on electrodes with different surface morphologies, Electrochem. Commun., 22 (2012) 16–20.
[67] A. Zeradjanina, F. Mantiab, J. Masaa, W. Schuhmann, Utilization of the catalyst layer of dimensionally stable anodes – interplay of morphology and active surface area, Electrochim. Acta, 82 (2012) 408–414.
[68] W. Sugimoto, T. Kizaki, K. Yokoshima, Y. Murakami, Y. Takasu, Evaluation of the pseudocapacitance in RuO_2 with a RuO_2/GC thin film electrode, Electrochim. Acta, 49 (2004) 313–320.
[69] H. Jeon, A. Dimas C. Permana, B. Min, J. Kim, Water splitting for hydrogen production using a high surface area RuO_2 electrocatalyst synthesized in supercritical water, Int. J. Hydrogen Energy, 38 (2013) 6092–6096.
[70] I. Chen, T. Chen, Y. Wei, C. Hu, T. Lin, Capacitive performance enhancements of RuO_2 nanocrystals through manipulation of preferential orientation growth originated from the synergy of Pluronic F127 trapping and annealing, Nanoscale, 6 (2014) 2861–2871.
[71] J. Ribeiro, A. Andrade, Characterization of RuO_2-Ta_2O_5 coated titanium electrode, J. Electrochem. Soc., 151 (2004) D106–D112.
[72] V. Jovanovic, A. Dekanski, P. Despotov, B. Nikolic, R. Atanasoski, The roles of the ruthenium concentration profile, the stabilizing component and the substrate on the stability of oxide coatings, J. Electroanal. Chem., 339 (1992) 147–165.
[73] T. Kishi, Y. Sugimoto, T. Nagai, Degradation behavior of a titanium supported RuO_2-TiO_2 electrode, Surf. Technol., 26 (1985) 245–251.
[74] L. Krstajic, T. Trisovic, N. Krstajic, Spectrophotometric study of the anodic corrosion of Ti/RuO_2 electrode in acid sulfate solution, Corros. Sci., 46 (2004) 65–74.
[75] L. Silva, K. Fernandes, L. Faria, J. Boodts, Electrochemical impedance spectroscopy study during accelerated life test of conductive oxides: Ti/(Ru + Ti + Ce)O_2-system, Electrochim. Acta, 49 (2004) 4893–4906.

Supplementary information

Fig. S3 shows the representative cyclic voltammograms of the macroporous RuO_2–TiO_2 electrodes (PS diameter of 0.1, 0.46, and 1.1 μm) and nontemplated electrode at two selected scan rates (5 mV/s (a) and 320 mV/s (b)) as cyclic voltammograms with various scan rate (5, 10, 20, 40, 80 160, and 320 mV/s) were measured to estimate voltammetric charge. As can be seen from Figs. S3(a) and (b), all CV curves show nearly rectangular shape indicating the good reversibility (redox reaction (1)) of the system resulting from the insignificant *i*R (ohmic drop) loss. The voltammetric charge (q) recorded over a potential range in the cyclic voltammogram can be described as a pseudo-capacitive reaction (reaction (1)) which consists of coupled redox transitions involving proton exchange at a broad reversible peak around 0.6 V vs. Ag/AgCl [50,51].

$$RuO_x(OH)_y + zH^+ + ze^- \rightarrow RuO_{x-z}(OH)_{y+z} \quad \text{(Reaction (1))}$$

Total or outer voltammetric charge can be obtained by varying the scan rate of the applied potential. The total voltammetric charge including both the inner and outer active surfaces can be measured at a low scan rate. On the other hand, the outer voltammetric charge can be obtained at a high scan rate [50,51]. This is explained as follows: at a low scan rate, the total active surface including both the inner and outer active surfaces can exchange protons with the solution, while at a high scan rate, the inner active surface fails to participate in this reaction. Thus, the total or outer active surface area can be estimated by plotting and extrapolating the voltammetric charge according to an infinitely low (0) and high (∞) scan rate with the following equations (Eqs. (1)–(3)) [51]:

$$q_{total} = q_{inner} + q_{outer} \quad (1)$$

$$q(v) = q_{outer} + A(1/\sqrt{v}) \quad (2)$$

$$1/q(v) = 1/q_{total} + B\sqrt{v} \quad (3)$$

where v is the scan rate; $q(v)$ is the voltammetric charge at the scan rate v; q_{total} is the voltammetric charge obtained at an infinitely low (0) scan rate; q_{outer} is the voltammetric charge obtained at a high (∞) scan rate; q_{inner} is related to the voltammetric charge of the inner surfaces; and A and B are constants.

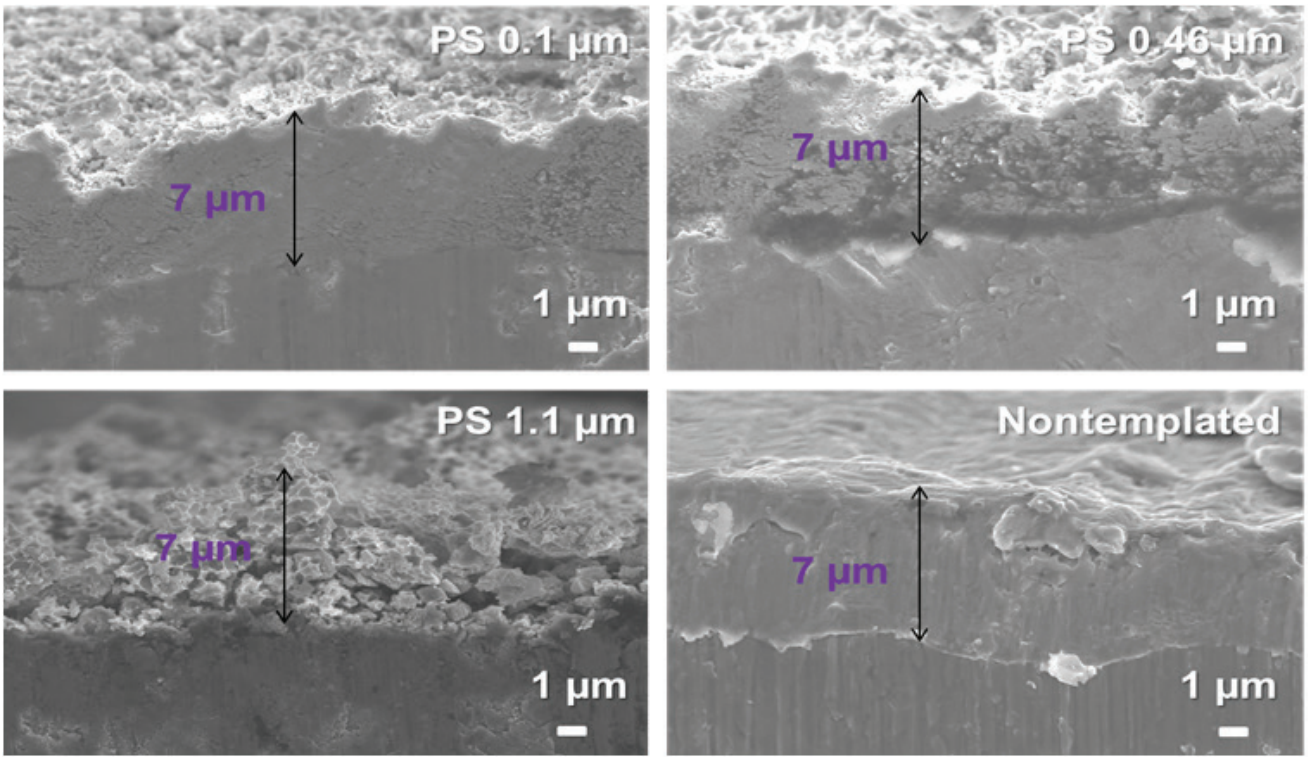

Fig. S1. Cross-sectional SEM images of the macroporous RuO_2–TiO_2 electrodes fabricated with several ranges of the PS sizes (diameter of 0.1, 0.46 and 1.1 μm) in comparison with that of the nontemplated RuO_2–TiO_2 electrode.

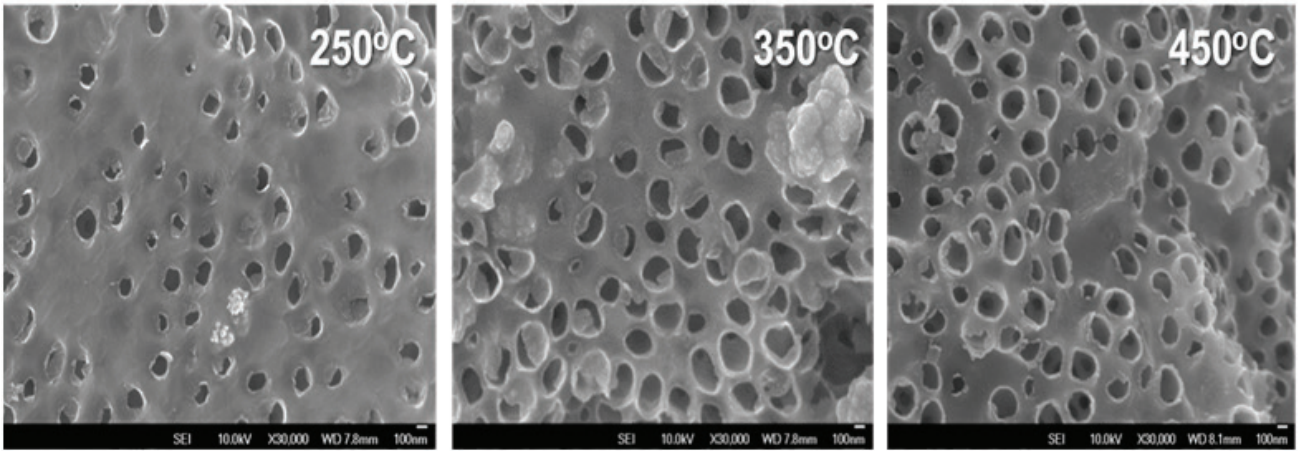

Fig. S2. SEM images of the macroporous RuO_2–TiO_2 electrodes (PS 0.46 μm template) fabricated at several calcination temperatures (250°C, 350°C, and 450°C).

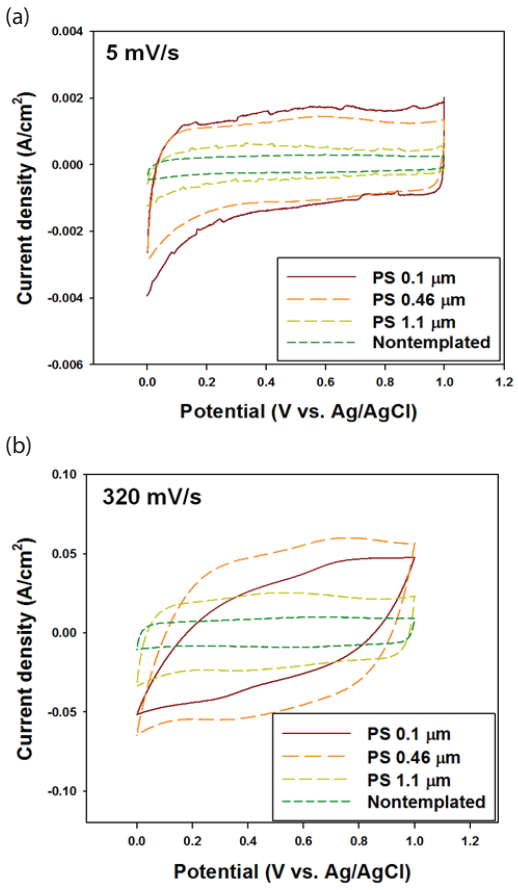

Fig. S3. Cyclic voltammograms of the macroporous RuO_2–TiO_2 electrodes fabricated with several ranges of the PS sizes (diameter of 0.1, 0.46 and 1.1 μm) and the nontemplated electrode at two selected scan rates (5 mV/s (a) and 320 mV/s (b)).

Table S1
Total and outer surface area of the macroporous RuO_2–TiO_2 electrodes fabricated with several ranges of the PS sizes (diameter of 0.1, 0.46 and 1.1 μm) in comparison with that of the nontemplated RuO_2–TiO_2 electrode

Electrode	Total voltammetric charge (mC/cm²)	Outer voltammetric charge (mC/cm²)
PS 0.1 μm	159	47
PS 0.46 μm	126	69
PS 1.1 μm	48	33
Nontemplated	27	16